On the oxidation mechanism of refractory high entropy alloys

Authors

Franz Müller[a], Bronislava Gorr[a], Hans-Jürgen Christ[a], Julian Müller[a], Benjamin Butz[a], Hans Chen[b], Alexander Kauffmann[b] and Martin Heilmaier[b]

Affiliation

[a]Institut für Werkstofftechnik, Universität Siegen, Siegen, Germany; [b]Institut für Angewandte Materialien, Karlsruher Institut für Technologie (KIT), Karlsruhe, Germany; [c]

Abstract

The high-temperature oxidation mechanism of a series of refractory high entropy alloys: TaMoCrTiAl, NbMoCrTiAl, NbMoCrAl and TaMoCrAl at 1000°C in air was studied. A complex protective oxide layer consisting of Al_2O_3, Cr_2O_3 and $CrTaO_4$ oxides was observed for the quinary Ta-containing alloy. The formation of $CrTaO_4$ in this alloy after a short incubation period decreased the oxidation kinetics from a parabolic to a quartic rate law. Ti was found to support the formation of $CrTaO_4$. In the Nb-containing alloys, the formation of different Nb_2O_5 polytypes near the metal/oxide interface caused a highly porous oxide scale and severe oxide spallation.

Keywords: Refractory high entropy alloy, High temperature corrosion, Compositionally complex alloy, Quartic rate law, $CrTaO_4$ formation

1. Introduction

The development of new high temperature structural materials is confronted with the common problem to realize a favourable combination of elevated temperature (creep and fatigue) strength, room temperature ductility and high temperature oxidation resistance in a single alloy. Recently, the discovery of novel multicomponent alloys, so-called High Entropy Alloys (HEAs) or Compositionally Complex Alloys (CCAs) has led to the development of a large number of new alloy systems with unique and, thus, attractive property combinations [1]. In contrast to the classical alloy design approach, HEAs do not have a certain base element but consist of five or more elements in nearly equimolar ratios. As a result, from a thermodynamic point of view, HEAs exhibit a higher mixing entropy compared to that of classical alloys which may suppress the formation of ordered intermetallic compounds and favour the formation of a single-phase with simple crystal structure instead. However, it was demonstrated recently, that this approach is by far too simple to predict single-phase HEAs and further physical and chemical effects have to be considered [2]. Rather, proper element selection is more important than the increase of the number of participating elements only [3, 4].

Recently, HEAs with high concentrations of refractory metals, typically greater than 50 at.%, have been suggested to possibly fulfill the initially mentioned property portfolio for high-temperature structural materials, mainly because of their high melting points, strength retention at elevated temperatures and reasonable room temperature ductility and toughness [5-7]. While microstructure and mechanical properties of refractory HEAs merit great attention among material scientists, studies on the oxidation behavior of these materials are still scarce [8]. Moreover, these studies often represent merely a cursory scan of alloy oxidation properties, in other words, the oxidation mechanisms are not thoroughly elucidated [9-11].

In classical metallurgical approaches, the oxidation resistance of high-temperature alloys relies on additions of Cr, Al and Si enabling the formation of protective Cr_2O_3, Al_2O_3 or SiO_2 scales. In

commercially available Ni-base and Fe-base high-temperature alloys, the concentrations of Cr, Al and Si usually do not exceed 25 at.% (e.g. the NiCrofer 3228 alloy), 11 at.% (B1914 alloy), 3.3 at.% (GX40CrSi29 alloy), respectively [12,13]. These (maximum) concentrations, on the one hand, ensure the formation of protective oxide layers and, on the other hand, guarantee that undesirable intermetallic phases such as Laves and Sigma phases as well as aluminides and silicides do not form. If such an alloy contains both, Cr and Al, the concentrations of these elements can be reduced as Cr and Al act synergistically and alloy passivation usually occurs very fast [14]. In many cases, small amounts of Si (max. 3 at.%) are added to further alleviate the formation of a protective chromia scale. In Nb- and Mo-based alloys, however, higher nominal concentrations of Si in conjunction with the formation of silicides as Si reservoirs are mandatory to form silica as a protective scale [15-17].

Obviously, decent oxidation resistance requires the addition of significant amounts of Al, Cr and possibly Si to HEAs. So far this has been scarcely done in literature [9-11, 18-22]. Our own exploratory work indicates the positive effects of Ta-substitution for Nb within the alloy system NbMoCrTiAl. In these preliminary studies, however, the mechanisms of oxidation behaviour were not fully rationalized [9, 11].

Based on these promising, albeit tentative results, we aim to elucidate the key role of the elements Ti, Nb and Ta on oxidation resistance by studying a systematic series of quaternary and quinary alloys. As a consequence, two equiatomic 5-component alloys (NbMoCrTiAl, TaMoCrTiAl) as well as two equiatomic quaternary alloys (NbMoCrAl, TaMoCrAl, i.e. without Ti), were studied. As a long-term objective, a more comprehensive understanding of the complex oxidation mechanisms may foster accelerated alloying strategies for oxidation resistant high strength refractory high entropy alloys.

2. Experimental Procedures

All alloys were cast from elemental bulk material by arc-melting (arc-melter AM 0.5 by Edmund Bühler GmbH) in ~0.6 atm. of Ar. The purities of the used elemental bulk materials Ta, Nb, Mo and Al were 99.9%, while Cr and Ti had purities of 99 % and 99.8%, respectively. The prepared buttons were flipped over and remelted at least five times in a water-chilled copper mold to facilitate alloy homogenization. All alloys were subsequently heat-treated at 1300-1400°C depending on alloy composition (see Tab.1) for 20 h in Ar atmosphere to dissolve the dendritic microstructure and achieve near-equilibrium microstructures at operating conditions. The alloys were cooled in the furnace after the heat treatment in (streaming) Ar atmosphere with a cooling rate of 4.2 K/min. The ingots were then cut by electrical discharge machining (EDM) to dimensions of 5 mm x 5 mm x 2 mm, polished up to grit P1200 and ultrasonically cleaned in ethanol directly before high-temperature exposure. Oxidation tests were carried out in a Rubotherm thermogravimetric system under isothermal conditions at 1000°C for 24 – 100 hours in laboratory air. To analyse the oxide morphology, a Focused Ion Beam - Scanning Electron Microscope (FIB-SEM) DualBeam system of type FEI Helios Nanolab 600 was used. It is equipped with techniques such as backscatter electron (BSE) imaging, energy-dispersive X-ray spectroscopy (EDX) as well as electron backscatter diffraction (EBSD). The mean oxide scale thickness and the mean depth of the internal corrosion zone of the investigated alloys after various exposure times were determined using three BSE cross-section images in each of which 20 individual measurements were carried out using the software ImageJ. The preparation of the pre-cut samples for transmission electron microscopy (TEM) was done by ion milling with Ga^+-ions at 5-30kV depending on the lamella thickness using the FEI Helios Nanolab 600. Subsequent TEM investigations were conducted using a TEM FEI Talos F200X with 200kV acceleration voltage. The crystal structures of the formed oxides in the surface scales were analysed by X-ray diffraction (XRD). These XRD measurements were carried out using an X'Pert Pro MPD diffractometer operating in Bragg-Brentano geometry with Cu-Kα radiation as described in Ref. [11]. Oxide scales formed on the alloys were removed mechanically from the oxidized

samples using a scalpel and pestled into powders with particle sizes smaller than 40 µm before XRD investigations.

3. Results

3.1 Microstructure

Figure 1 exemplifies the microstructure of the four investigated alloys after suitable annealing as given in Table 1. None of the alloys is entirely single-phase after annealing. Specifically, the alloys NbMoCrAl and TaMoCrAl exhibit a noticeable amount of secondary, intermetallic phases which were subsequently characterized by combined EDX and EBSD (Figs. 2 a.,b.) as well as XRD analysis (see supplementary materials Figs. S1 a, b). The powder XRD measurements of both alloy NbMoCrAl and TaMoCrAl revealed a C14-type Laves phase (Cr_2Ta/Cr_2Nb) and an A15 phase ($AlMo_3$/ $Al(Mo, Nb)_3$) (Figs. S1 a, b). Further, ordering of the bcc solid solution (A2) towards a B2-type crystal structure of is assumed; this is indicated by the exclusive B2 superlattice peaks (open diamonds) in the supplementary materials Figs. S1. In agreement with the XRD measurements, the EDX and EBSD results (Fig. 2) confirm the presence of C14-type Laves phase in both alloys, however reliable identification between the cubic A15, A2 and B2 phases seems difficult during automated acquisition and indexing of EBSD patterns.

The microstructure investigations of both quinary alloys NbMoCrTiAl and TaMoCrTiAl were already published in our latest works [11, 23] and are, thus, only summarized shortly. In contrast to the quaternary alloys, only minor amounts of both i.e. A15 and C14 secondary phases were observed for NbMoCrTiAl, appearing as a fringe of tiny dimensions in the vicinity of some grain boundaries (see Fig. 1). Large grains with an ordered B2-type crystal structure were observed by TEM measurements as presented in our other work [23]. The alloy TaMoCrTiAl, however, showed after annealing at 1400°C for 20h merely Cr_2Ta Laves phase (20% area fraction) of C14-type (Tab. 1), predominantly located at grain boundaries, but no evidence of the A15 phase [11]. Volume fractions of the studied alloys were assessed by BSE-contrast or EBSD measurements if possible and are listed in Tab. 1.

3.2 Oxidation kinetics

In Figs. 3 a-b, the mass change versus time curves of the alloys NbMoCrAl, NbMoCrTiAl, TaMoCrAl, TaMoCrTiAl during isothermal exposure in air at 900-1100°C are displayed. The mass change during isothermal exposure can be rationalized through:

$$(\Delta W/A)^n = k \cdot t \qquad (1)$$

where ΔW/A is the mass change per unit area, t the exposure time, n the oxidation rate exponent and k the oxidation constant. A linear plot of $(\Delta W/A)^n$ vs. t yields the oxidation constant k as the slope of the straight. From a logarithmic representation of this relation the rate exponent (n) can be derived according to

$$\ln \Delta W/A = \frac{1}{n} \ln k + \frac{1}{n} \ln t \qquad (2)$$

as the slope of a double logarithmic plot of mass change versus time. This is depicted for the investigated alloys at 1000°C in air in Figs. 4a and b and the corresponding n and k values are listed in Tab. 2. Both Ta-containing alloys, Fig. 3a, exhibited the lowest mass gain during oxidation at 1000°C. In the early oxidation stage (t=0.5-4.5h), TaMoCrTiAl showed mass gain with a parabolic rate (n=1.82) which later

on decreased to a quartic oxidation rate (t=4.5h-100h, n=4.55) yielding a very low mass gain up to 300h (see Fig. 3a). Interestingly, the Ti-free alloy TaMoCrAl behaved differently with oxidation kinetics obeying a quartic rate law at the very beginning (t= 0.14h-3h, n= 4.35), subsequently increasing towards a parabolic oxidation rate (t= 3h-48h, n= 2.08). After 48h of exposure, the TaMoCrAl alloy showed an abrupt increase in oxidation rate, similar to break-away behavior which resulted in complete oxidation of the sample after 100h oxidation (see Fig. 3a).

Both Nb-containing alloys (Fig. 3b) generally exhibited substantially higher mass changes and different oxidation kinetics compared to those of the Ta-containing alloys. The oxidation kinetics of NbMoCrTiAl increased from near-parabolic kinetics (t= 0.17h-8.17h, n=1.49) to linear one (n=0.82) during exposure in air at 1000°C (see Tab. 2). For the Ti-free NbMoCrAl, the decrease of oxidation rate exponent was even more pronounced from n=2.08 to n=0.30 after 7h of exposure to air at 1000°C. Further, after 24h of oxidation, the mass gain suddenly stopped and subsequent mass loss was observed. After 48h of exposure to air at 1000°C, the complete sample of NbMoCrAl was oxidized and no residual metal substrate could be found.

In agreement with the thermogravimetric analyses, inspection of the formed oxide layers of both Ta-containing alloys yielded these to be substantially thinner compared to those on the Nb-containing variants (see Fig.5a). In addition, the internal corrosion process for both Ta-containing alloys proceeded distinctly slower during the first 24h compared to NbMoCrTiAl and NbMoCrAl (Fig. 5b). As described further below, the internal corrosion zone was defined as the area below the oxide scale where corrosion products, mainly Al_2O_3, CrN and TiN were detected. For the NbMoCrAl and NbMoCrTiAl alloys, the internal corrosion zone thickness is interestingly reduced or even disappeared after more than 3h (see Fig. 5b.); this zone was rarely detected in the cross-sectional images.

According to Fig. 4 and Table 2, oxidation rates of the two Nb-containing alloys are low at the beginning of the oxidation process indicating the formation of relatively protective scales. In turn, the precipitation of corrosion products in the metallic substrate which were predominately Al_2O_3 or TiN is facilitated (as shown in Figs. 6 and 7). When the oxide scales become non-protective and the oxygen partial pressure below the oxide scale increases, residual metal and nitrides in the internal corrosion zone were oxidized. Obviously, the oxidation process became dominant compared to the internal corrosion, i.e. nitridation, after prolonged oxidation.

3.3 Microstructural analysis of oxide scales

3.3.1. NbMoCrTiAl and NbMoCrAl

As a follow up of our preliminary results [9], we will focus here on elucidating the high-temperature oxidation mechanism of the Nb-containing HEAs during short term and long term exposure in air up to 100h at 1000°C. Three oxides were identified after 48h oxidation at 1000°C by powder XRD measurements: Rutile, corundum and Nb_2O_5 (see supplementary materials Fig. S2). According to our Rietveld analyses [9], rutile was the dominant oxide phase which formed during high-temperature oxidation at 1000°C and the volume fractions of the other oxides were much lower (being around 15 Vol.% after 48h) [9]. In Figs. 6a-c, the BSE cross-section images of NbMoCrTiAl present the course of the complex oxide layer formation after exposure to air for 3h, 48h and 100h, respectively, at 1000°C. Figure 6d exemplifies the EDX analysis of this alloy after oxidation for 48h. Already after 3h (Fig. 6a) both, a sequence of thick and thin oxide layers was observed. The thick sublayers are enriched in Nb and contain pores and cracks. The thin parts exhibit a dense multi-layer structure with Ti-, Al- and Cr-rich oxides. After 48h of oxidation, similar results were observed [9]. Concerning the thin oxide layers (see the outermost part of the scale in Fig. 6b) pure rutile TiO_2 was identified by XRD and EDX (see also supplementary material Fig. S2.). Underneath, in the order from outside to inside, a multi-layer

consisting of Al_2O_3, Cr_2O_3, Nb_2O_5 and $CrNbO_4$ oxides was identified (Figs. 6). Below the oxide scale, internal corrosion products like fine Al_2O_3 particles and predominately coarse, spherical TiN particles are found (Fig. 6 b.), of which the phases were confirmed by previous XRD measurements [9]. After 100h of oxidation (Fig. 6c), thick and porous multiphase oxide scales of mostly rutile-type oxide layers are present, whereas the internal corrosion zone appears much thinner (compared to Fig. 5b) and only fine TiN and Al_2O_3 particles were observed (not presented here).

To study the importance of Ti for oxidation resistance in this alloy system, samples of Ti-free equimolar alloy NbMoCrAl were oxidized under similar conditions at 1000°C in air. Different to NbMoCrTiAl, a substantial amount of the intermetallic phases A15 and Laves phases (see. Tab. 1) was found after heat-treatment in NbMoCrAl which may impact scale formation.

XRD-analysis after 3h of exposure (not shown here) reveals the formation of the following oxides: corundum-type chromia and alumina, rutile-type solid solutions of MO_2 with major solvents of M=Cr, Mo, Nb but also pure Nb_2O_5 oxides. No further oxides are found after prolonged oxidation times, however, the intensity of the rutile-type oxide increased compared to corundum-type oxide.

Fig. 7 exemplifies BSE-images of NbMoCrAl after 3h and 24h of exposure to air at 1000°C. After 3h of exposure, the 4.6 +/- 0.5µm thick scale essentially contains oxides of MO_2 rutile-type solid solutions and to a lesser extent of Nb_2O_5 and Cr_2O_3 (Fig. 7a). Further precipitates of alumina forming a sparse scale within the rutile-type layer were identified. Below the oxide scale, the EDX and XRD investigations reveal the formation of Al_2O_3 and Cr_2N, generally located at the phase boundaries and within the grains of the Cr_2Nb Laves phase (Fig. 7a).

After 24h, the structure of consecutive layers within the scale is clearly seen (see Fig. 7b). Between the layers, significant porosity is observed that apparently led to delamination of layers. The layers consist of alternating rutile, Nb_2O_5, and Cr_2O_3 as well as semi-continuous layers with Al_2O_3. Severe crack formation and spallation occurred in the Nb_2O_5-rich layers and at the metal/oxide interface (see the lower area in Fig. 7b). Interestingly, the amount of internal nitridation was clearly reduced after prolonged oxidation time and no corrosion products were found below the oxide scale (see Fig. 7c).

3.3.2 TaMoCrTiAl and TaMoCrAl

The XRD-measurements of TaMoCrTiAl after 3h and 300h of oxidation at 1000°C in air (Fig. 8) both yield the formation of titania, alumina, chromia and $CrTaO_4$. In order to investigate the corrosion products in detail, TEM analyses were performed on a sample oxidized for 3h at 1000°C (see supplementary materials Fig. S3). A multi-layered oxide scale consisting of outer TiO_2, Al_2O_3, Cr_2O_3 and inner $CrTaO_4$ could be confirmed. Several round-shaped Al_2O_3 precipitates below the oxide scale and within the Laves phase were identified by EDX measurements and TEM diffraction patterns (displayed in supplementary materials Fig. S3 b-d).

Figure 9 displays the cross-section BSE images after 48h (a), 100h (b) and 300h (c) of oxidation at 1000°C in air and an enlarged EDX-mapping (d) of the zone framed in dashed lines in (a). By combination of the EDX and XRD investigations (also see Fig. 8), it was found that the oxide scale composition during 3h till 300h of exposure to air was comparable. As demonstrated in the EDX mapping in Figure 9d, titania was formed as the top layer, alumina and chromia were identified underneath. The inner layer consisted of $CrTaO_4$ which became clearly thicker (approx. 8µm) with oxidation time, whereas the other layers remained unchained (compare Fig. 9a-c).

Since several oxide layers formed during oxidation, it is mandatory to explore which of these oxides may finally be responsible for the high oxidation resistance of the alloy TaMoCrTiAl. While Al_2O_3 and

Cr_2O_3 are generally considered as protective oxides in literature, little is known about the protectiveness of $CrTaO_4$. Hence, to study this, the alloy TaMoCrTiAl was oxidized in a separate discontinuous experiment for 6h at 1000°C. Subsequently, the upper oxide scale consisting of TiO_2, Al_2O_3 and Cr_2O_3 was removed by mechanical grinding leaving a thin $CrTaO_4$ layer on the surface (see Fig. 10a). Then, the oxidation of the sample continued in air at 1000°C for 24h (see Fig. 10b). The BSE cross-section images reveal that no additional oxides were observed on top of the (now "outermost") $CrTaO_4$ layer (see Fig. 10b). Only the thickness of the $CrTaO_4$ layer and of the internal corrosion zone, containing mostly Ti-nitrides and alumina, increased by 4 µm and 14 µm, respectively. This suggests that the outward diffusion of cations through the $CrTaO_4$ layer was clearly inhibited, while the inward diffusion of oxygen and nitrogen was not suppressed. It can, therefore, be assumed that the metallic substrate is effectively protected by the slow growth of $CrTaO_4$ which explains the lower oxidation rates of both Ta-alloys compared to the Nb-alloys (see Tab. 2).

To evaluate the importance of Ti on the high temperature oxidation resistance on TaMoCrTiAl, we comparatively investigated the quaternary Ti-free TaMoCrAl alloy being exposed to air at 1000°C for up to 100h. The XRD measurements after 3h of oxidation (see supplementary materials Fig. S4) identified various oxides: Cr_2O_3, Al_2O_3 and $CrTaO_4$. After 48h of oxidation, also Ta_2O_5 was found in XRD investigations (not shown here).

In Figures 11a-b, the BSE cross-section images of TaMoCrAl after 3h and 48h exposure to air at 1000°C are displayed. The average oxide layer thickness after 3h oxidation was only 2.1 µm and the layers appeared adherent with no or minor visible pores or cracks. EDX investigations (not presented here) and XRD measurements (see supplementary materials Fig. S3) revealed the formation of an upper layer consisting of Cr_2O_3 and Al_2O_3, as well as a thicker inner scale of $CrTaO_4$ (Fig. 11a).

In contrast, after 48h of exposure, a much thicker (28.5µm in average) and porous oxide scale was observed (Fig. 11b). The outermost layer with a darker contrast in the BSE image is comprised of thin Cr_2O_3 and Al_2O_3 oxides; see Fig. 11b. The inner layer, though, shows a multi-phase structure consisting essentially of $CrTaO_4$ and Ta_2O_5 with semi-continuous scales of Cr_2O_3 and Al_2O_3 which appear in a darker contrast in the BSE cross-section image (as shown in Fig. 11b). Below the thick oxide scale, pronounced internal oxidation was additionally observed, especially at the phase boundaries which were decorated with alumina and Cr_2N particles (Fig. 11b).

4. Discussion

The results presented above clearly reveal a higher oxidation resistance for both Ta-containing alloys and inferior oxidation behavior for both Nb-containing alloys during exposure to air at 1000°C. Ta, Nb and Ti, which are present in relatively high concentrations (20 at.% in quinary and 25 at.% in quaternary alloys, respectively) in the studied alloys, obviously have a pronounced effect on the elevated temperature oxidation resistance.

The formation of the multi-layered oxide scales as observed in our experiments can be rationalized taking into account both, thermodynamic and kinetic aspects. In doing so, standard free energies of formation of the observed oxides at 1000°C were calculated using the commercial software FactSage. The formation of $CrTaO_4$ and $CrNbO_4$ oxides below the chromia and alumina layers was observed for the Ta- and Nb-containing alloys, respectively. Assuming the chemical reactions (3) and (4) according to [24], the standard free energies of formation of $CrTaO_4$ and $CrNbO_4$ were calculated as described in eqs. (5) and (6). The calculated ΔG^0 values are summarized in Tab.3.

$$1/2\ Cr_2O_3(s)+1/2\ Ta_2O_5\ (s) = CrTaO_4\ (s) \qquad (3)$$

$$1/2\ Cr_2O_3\,(s)+1/2\ Nb_2O_5\,(s) = CrNbO_4(s) \quad (4)$$

$$\Delta G^0_{CrTaO4} = 1/2\ (\Delta G^0_{Cr2O3} + \Delta G^0_{Ta2O5}) \quad (5)$$

$$\Delta G^0_{CrNbO4} = 1/2\ (\Delta G^0_{Cr2O3} + \Delta G^0_{Nb2O5}) \quad (6)$$

According to Tab.3, the thermodynamic driving forces are highest for Al_2O_3 and TiO_2 amongst all considered oxide species, which result in the formation of an initially multi-layered oxide scale, consisting of the outer TiO_2 and the inner Al_2O_3. According to Fig. 10, though, these oxides seem to be a product of the transient oxidation only, and do not significantly influence the further oxidation process.

Generally, the impact of Ti on the oxidation resistance seems to be positive. Although the experiments with the Ti-free alloys NbMoCrAl and TaMoCrAl first indicate superior, i.e. slower, oxidation kinetics during initial oxidation as compared to their Ti-containing counterparts (see Fig. 3), after longer oxidation times the oxide scales of both Ti-free alloys were thicker and less adherent (Fig. 5). This is believed to be the effect of higher Mo-concentrations in the Ti-free alloys and, consequently, the higher volume fraction of the Mo-rich A15 phase (see Fig. 1) which is known to be intrinsically not oxidation resistant [25, 26]. The oxidation of the A15 phase causes the formation of volatile Mo-oxides, which have a destructive effect on the macroscopic integrity of the initially protective oxide scale. As a further consequence, the oxide scales which formed at prior A15 phase grains eventually became porous evoking even severe evaporation of Mo-oxides (Fig. 2).

Though the elements Nb and Ta are known to have a similar chemical nature, their effect on the oxidation behavior of the studied alloys is seemingly different. As the thermodynamic stability of $CrNbO_4$ is almost the same as those of Cr_2O_3 and Nb_2O_5 (Tab. 3), this may apparently lead to a competition in the formation between these oxides that can explain an only partial formation of $CrNbO_4$. In contrast, the thermodynamic stability of $CrTaO_4$ is clearly higher as of Cr_2O_3, thus the formation of distinct and protective $CrTaO_4$ layers below Cr_2O_3 is facilitated. $CrNbO_4$ oxides, however, have been found to improve the oxidation resistance of various other alloys, e.g. Nb-Si-based alloys [27, 28.]. Chan et al. reported enhanced thermal cycling oxidation resistance of Nb-Cr-Si-based alloy due to the formation of adherent $CrNbO_4$ layers instead of Nb_2O_5 [29]. Qu et al. reported on enhanced adherence between oxide scale and substrate of Nb-Si based alloys due to $CrNbO_4$ formation at the metal/oxide interface [30]. One can, therefore, expect a relatively high oxidation resistance of an alloy forming $CrNbO_4$.

In our study, both Nb-containing alloys first showed almost parabolic oxidation kinetics with rate exponents of n=1.49-2.0 suggesting the initial formation of protective oxide layers such as $CrNbO_4$, Cr_2O_3 and Al_2O_3. However, a severe increase of oxidation rates and high mass gain after prolonged oxidation time indicate porous, fast-growing non-protective oxide scales (Tab 2). As illustrated schematically in Fig. 12, the increase of the oxidation rates observed for both Nb-containing alloys can be attributed to the formation of various polymorphic forms of Nb_2O_5 which have been identified by XRD (supplementary materials Fig. S2) and EBSD (not presented here).

Especially at temperatures below 1100°C, various monoclinic and orthorhombic polymorphs have been observed which transform rapidly at temperatures above 1100°C to monoclinic H-Nb_2O_5, the stable high-temperature form [31, 32]. In the intermediate temperature range between 1000-1100°C, the formation of different Nb_2O_5 polymorphs will lead to severe anisotropic volume expansion and, thus, to crack formation. In our findings, at least two polymorphic forms of Nb_2O_5 have been identified by EBSD and XRD, namely h-Nb_2O_5 and β-Nb_2O_5 (supplementary materials Fig. S2). Among all these, β-Nb_2O_5

is known to be the most expanding Nb_2O_5 [27, 28, 33-35]. It is thus, by no means surprising that crack formation occurs at the interphase substrate/oxide (Fig. 12), hence leading to rapid oxygen ingress and explains the observed massive increase of mass gain (see Fig. 3), oxidation rates(see Tab. 2) and oxide scale growth (see Fig. 5) of both Nb-containing alloys. Consequently, the alloy with the highest Nb content (NbMoCrAl) exhibited the worst oxidation resistance and formed the thickest Nb-rich oxide scales (see Fig. 5). The effect of the Cr_2Nb Laves phase on the oxide layer formation is rather small: the oxide layer formed on top of the Laves phase grains had a similar thickness as that one formed on top of the other phases. However, the effect of the Laves phase on internal corrosion is significant. First, Al_2O_3 precipitates seem to form primarily in the Laves phase rather than in the matrix. A similar experimental finding was observed in the alloy TaMoCrTiAl (see supplementary material Fig. S3). Second, internal corrosion starts at the phase boundaries as TiN and CrN precipitations were abundantly found between the Laves phase and the matrix (Figs. 6a and 7a).

The $CrTaO_4$ oxide, identified during oxidation experiments of Ta-containing alloys, is supposed to form by the reaction, eq. 3, and, thus, first requires an incubation period for the formation of Cr_2O_3 and Ta_2O_5. It should be noted, however, that no pure Ta_2O_5 was observed for TaMoCrTiAl by XRD-analysis possibly due to the very fast reaction to $CrTaO_4$. Ta_2O_5, though forming rapidly growing scales with PBR values of 2.5 [36], is stable only as monoclinic α-Ta_2O_5 up to 1350°C in contrast to Nb_2O_5 that yields numerous polymorphic modifications. Therefore, the oxide scales formed on Ta-containing alloys (see. Fig. 10) generally show a better adherence compared to Nb_2O_5-forming alloys. After forming Ta-rich oxide scales it is rather unexpected that the alloy TaMoCrAl finally exhibits break-away oxidation after prolonged oxidation (see Fig. 11). We attribute this to the above-described formation of the Mo-rich A15 phase in the alloy TaMoCrAl (see Fig. 2) which led to enhanced formation of volatile Mo-oxides resulting in damaging the initially protective oxide scales (see Fig. 3). The influence of the Cr_2Ta Laves phase on the oxidation resistance on both, microscopic and macroscopic level, is similar to that discussed for the alloy NbMoCrTiAl

Besides the positive effect of the Ti-addition on suppressing the formation of the A15 phase, Ti obviously plays a beneficial role by decreasing the amount of less favourable Ta_2O_5 (or Nb_2O_5) and increasing the fraction of more favourable Ti-rich rutile-type solid solutions. Interestingly, various Ti-, Cr-, Ta- and Nb- oxides are known to form highly stable rutile phases and mixed solid solutions like TiO_2 (ICSD: 9161), TaO_2 (ICSD: 7624), $CrTaO_4$ (ICSD: 72276), ,$TaTiO_4$ (ICSD: 72278), CrNbO4 (ICSD: 72275) and $(Cr,Ti,Ta)O_6$ (ICSD: 160795) to mention few of them. The PBR value of rutile-type TiO_2 generally is more favorable (1.7) [36], therefore the Ti-rich rutile-type oxides show improved adherence compared to Nb_2O_5 or Ta_2O_5 based oxide scales.

The high-temperature oxidation kinetics for the formation of protective alumina or chromia layers is known to obey parabolic oxidation kinetics [12, 37]. The observed oxidation kinetics and oxide scale growth for the Ta-containing alloys, however, suggests the formation of a similarly highly protective oxide scale. After an incubation period that corresponds to the observed first 4.5h for TaMoCrTiAl, very low oxidation rates according to a quartic rate law were observed (see Tab. 2). The experiments further present that oxygen inward diffusion through the $CrTaO_4$ scale is rate-determining (see Fig. 9). The above-mentioned conclusions on the oxidation behavior of TaMoCrTiAl and TaMoCrAl are illustrated schematically in Fig. 13.

Recently Ren et al. reported on the enhanced oxidation resistance of Ni-based superalloys between 850 and 900°C in air due to the formation of $CrTaO_4$ oxides that form below Cr_2O_3 oxides after a short incubation time. The oxidation rate constants published by Ren et al. can be compared with the ones of our TaMoCrTiAl alloy in the temperature range 900-1100°C (see Tab. 2) [11]. Comparing the logarithm of oxidation rate constants of rutile-type $CrTaO_4$ comparable activation energies for the oxidation

process of Q=350 kJ/mol for TaMoCrTiAl and Q=375 kJ/mol for Ni-based alloy [38] can be accessed(see Fig. 14). Considering the activation energies for chromia (250 kJ/mol) [39] and alumina forming Ni-based superalloys (400 kJ/mol) [40], it can be stated that the activation energy for oxygen diffusion through $CrTaO_4$ and oxidation rate constant obviously lie in between, but advantageously closer to that of alumina.

5. Conclusions

Systematic comparative investigations of the oxidation behaviour of four refractory HEAs within the system Ta-Nb-Mo-Cr-Ti-Al in a temperature range between 900 and 1100°C lead to the following conclusions:

(i) The superior oxidation resistance of TaMoCrTiAl at 1000°C in air is the result of the formation of protective Al_2O_3, Cr_2O_3 and $CrTaO_4$ oxide layers. The slow oxygen diffusion through $CrTaO_4$ seems to be rate determining which may pave the way for further development of oxidation-resistant refractory HEAs.

(ii) Although the initial formation of similar protective oxide layers consisting of Al_2O_3, Cr_2O_3 and $CrNbO_4$ were observed for NbMoCrTiAl and NbMoCrAl, the highly and anisotropic thermal expansion of the Nb_2O_5 polymorphs leads to pore formation and scale spallation.

(iii) Ti-addition plays a crucial role in forming protective rutile type oxides (like $CrTaO_4$), simultaneously decreasing the amount of less favorable oxides (Nb_2O_5, Ta_2O_5). Further, the volume fraction of the A15 phase can be reduced or even completely suppressed by the Ti-addition.

In our future works, the effect of Y additions aiming at the enhancement of oxidation resistance of NbMoCrTiAl alloy will be investigated. The oxidation behavior of both Ta-containing alloys is very promising, however, concerning the mechanical properties, the amount of brittle intermetallic compounds such as Laves Phases should be reduced. Therefore, the reduction of Cr- and Ta-concentrations in the TaMoCrTiAl system will be undertaken. The alloys with reduced Cr- and Ta-concentrations will be studied in terms of their microstructure and high-temperature corrosion behavior.

Data availability

The data that support the finding of this study are available as supplementary materials or from the corresponding author upon reasonable request.

Acknowledgment

The financial support by the Deutsche Forschungsgemeinschaft (DFG), grant no. GO 2283/2-1 and GO 2283/4-1, is gratefully acknowledged. Part of this work was performed at the Micro- and Nanoanalytics Facility (MnaF) of the University of Siegen.

Appendix A. Supplementary material

Supplementary material related to this article can be found in the attachment.

References

[1] Yeh J, Chen YL, Lin SJ, et al. High-entropy alloys – a new era of exploitation, Mater. Sci. Forum 560 (2007) 1–9.

[2] F. Otto, Y. Yang, H. Bei and E.P. George, Relative effects of enthalpy and entropy on the phase stability of equiatmoic high-entropy alloys, Acta Mater. 61 (2013) 2628-2638

[3] Z. Wu, H. Bei, F. Otto, G. M. Pharr, E. P. George, Recovery, recrystallization, grain growth and phase stability of a family of FCC-structured multi-component equiatomic solid solution alloys, Intermetallics 46 (2014) 131-140

[4] D. B. Miracle, O.N. Senkov, A critical review of high entropy alloys and related concepts, Acta Mater. 122 (2017) 448–511.

[5] O. N. Senkov, S.V. Senkova, D.M. Dimiduk, C. Woodward, D.B. Miracle, Oxidation behavior of a refractory NbCrMo0.5Ta0.5TiZr alloy, J. Mater. Sci. 47 (2012) 6522–6534.

[6] O. N. Senkov, S. V. Senkova, C. Woodward, D. B. Miracle, Low-density, refractory multi-principal element alloys of the Cr–Nb–Ti–V–Zr system: microstructure and phase analysis, Acta Mater. 61 (2013) 1545–1557

[7] O. N. Senkov, C. Woodward, D. B. Miracle, Microstructure and Properties of Aluminium-Containing Refractory High Entropy Alloys, JOM 66 (2014) 2030-2042

[8] O. N. Senkov, D. Miracle, K. Chaput, J. Couzinie, Development and exploration of refractory high entropy alloys—A review. J. Mater. Res. (2018) 1-37.

[9] B. Gorr, F. Müller, H.-J. Christ, T. Müller, H. Chen, A. Kauffmann, M. Heilmaier, High temperature oxidation behaviour of an equimolar refractory metal-based alloy 20Nb-20Mo-20Cr-20Ti-20Al with and without Si addition, J. Alloys Compd. 688 (2016) 468-477

[10] B. Gorr, F. Mueller, M. Azim, H.-J. Christ, T. Mueller, H. Chen, A. Kauffmann, M. Heilmaier, High-Temperature Oxidation Behavior of Refractory High-Entropy Alloys: Effect of Alloy Composition, Oxid. Met. 88 (2017) 339-349

[11] F. Müller, B. Gorr, H.-J. Christ, H. Chen, A. Kauffmann, M. Heilmaier, Effect of microalloying with silicon on high temperature oxidation resistance of novel refractory high-entropy alloy Ta-Mo-Cr-Ti-Al, Mater. High Temp. 35 (2018) 168–176.

[12] D. J. Young, High Temperature Oxidation and Corrosion of Metals, second ed., Elsevier Science, Amsterdam, 2016.

[13] R. Bürgel, Handbuch Hochtemperatur-Werkstofftechnik, fourth ed., Springer Vieweg, Wiesbaden, 1998

[14] E. Scheil, E. H. Schulz, Hitzebeständige Chrom-Aluminium-Stähle, Arch. Eisenhüttenwes. 6 (1932) 155–160

[15] D. Schliephake, M. Azim, K. Von Klinski-Wetzel, B. Gorr, H.-J. Christ, H. Bei, E. P. George, M. Heilmaier, High-Temperature Creep and Oxidation Behavior of Mo-Si-B Alloys with High Ti Contents, Metall. Mater. Trans. A 45 (2014) 1102-1111

[16] M. Azim, S. Burk, B. Gorr, H.-J. Christ, D. Schliephake, M. Heilmaier, R. Bornemann, P. H. Bolivar, Effect of Ti (Macro-) Alloying on the High-Temperature Oxidation Behavior of Ternary Mo-Si-B Alloys at 820-1300°C, Oxid. Met. 80 (2013) 231-242

[17] A. Vazquez, S. K. Varma, High-temperature oxidation behavior of Nb-Si-Cr alloys with Hf additions, J. Alloys Compd. 509 (2011) 7027-7033

[18] T. M. Butler, K. J. Chaput, J.R. Dietrich, O. N. Senkov, High temperature oxidation behaviors of equimolar NbTiZrV and NbTiZrCr refractory complex concentrated alloys (RCCAs), J. Alloys Compd. 729 (2017) 1004-1019

[19] N. D. Stepanov, D.G. Shaysultanov, G.A. Salishchev, M.A. Tikhonovsky, Structure and mechanical properties of a light-weight AlNbTiV high entropy alloy, Mater. Lett. 142 (2015) 153-155

[20] N. D. Stepanov, N.Y. Yurchenko, D.V. Skibin, M.A. Tikhonovsky, G.A. Salishchev, Structure and mechanical properties of the AlCrxNbTiV (x 5 0, 0.5, 1, 1.5) high entropy alloys, J. Alloys Compd. 652 (2015) 266-280

[21] Y. Liu, Y. Zhang, H. Zhang, N. Wang, X. Chen, H. Zhang, Y. Li, Microstructure and mechanical properties of refractory HfMo0.5NbTiV0.5Six high-entropy composites, J. Alloys Compd. 694 (2017) 869-877

[22] N. N. Guo, L. Wang, L.S. Luo, X.Z. Li, R.R. Chen, Y.Q. Su, J.J. Guo, H.Z. Fu, Microstructure and mechanical properties of refractory high entropy (Mo0.5NbHf0.5ZrTi)BCC/M5Si3 in situ compound, J. Alloys Compd. 660 (2016) 197-203.

[23] H. Chen, A. Kauffmann, B. Gorr, D. Schliephake, C. Seemüller, J. N. Wagner, H.-J. Christ, M. Heilmaier, Microstructure and mechanical properties at elevated temperatures of a new Al-containing refractory high-entropy alloy Nb-Mo-Cr-Ti-Al, J. Alloys Compd. 661 (2016) 206-215.

[24] P. Massard, J. C. Bernier, A. Michel, Effet Jahn-Teller dans le système Ta2CrO6-TaCrO4, J. Solid State Chem. 4 (1972) 269–274.

[25] F. Rioult, R. Sakidja, J. H. Perepezko, J. H. Coating strategies for oxidation resistant high temperature Mo-Si-B alloys, ECS Trans. 3 (2007) 113–127.

[26] J. Zhou, M. Taylor, G. A. Melinte, A. J. Shahani, C. C. Dharmawardhana, H. Heinz, P. W. Voorhees, J. H. Perepezko, K. Bustillo, P. Ercius, J. Miao, Quantitative characterization of high temperature oxidation using electron tomography and energy-dispersive X-ray spectroscopy, Sci. Rep. 8 (2018) 1-8.

[27] K. S. Thomas, S. K. Varma, Oxidation response of three Nb–Cr–Mo–Si–B alloys in air, Corr. Sci. 99 (2015) 145–153

[28] N. Esparza, V. Rangel, A. Gutierrez, B. Arellano, S.K. Varma, A comparison of the effect of Cr and Al additions on the oxidation behaviour of alloys from the Nb–Cr–Si system, Mater. High Temp. 33 (2016) 105–114

[29] K. S. Chan, Cyclic oxidation response of multiphase niobium-based alloys, Metall. Mater. Trans. A 35 (2004) 589–597

[30] S. Y. Qu, Y. F. Han, J. X. Song, Y. W. Kang, Effects of Cr and Al on high temperature oxidation resistance of Nb-Si system intermetallics, Mater. Sci. Forum 546-549 (2007) 1485–1488.

462 [31] J. Spyrdelis, O. Delavignette, S. Amelinckx, on the superstructures of Ta2O5 and Nb2O5, phys.
463 stat. sol. 19 (1967) 683-704

464 [32] H. Schäfer, R. Gruehn, F. Schulte, The Modifications of Niobium Pentoxide, Angew. Chem Int
465 Ed. Engl. 5 (1966) 40–52

466 [33] S. K. Varma, C. Parga, K. Amato, J. Hernandez, Microstructures and high temperature oxidation
467 resistance of alloys from Nb–Cr–Si system, J. Mater. Sci. 45 (2010) 3931–3937.

468 [34] M. P. Arbuzov, V. G. Chupria, The oxidation of niobium and the structure of niobium oxides, Sov.
469 Phys. J. 8 (1965) 87–89

470 [35] T. S. Ercit, Refinement of the structure of z-Nb_2O_5 and its relationship to the rutile and thoreaulite
471 structures, Mineral Petrol 43 (1991) 217–223

472 [36] N. B. Pilling, R. E. Bedworth, The Oxidation of Metals at high Temperatures. J. Inst. Met. 29 (1923)
473 529–591.

474 [37] P. Kofstad, High-temperature oxidation of metals, John Wiley & Sons, INC., New York, 1966

475 [38] W. Ren, F. Ouyang, B. Ding, Y. Zhong, J. Yu, Z. Ren, L. Zhou, The influence of CrTaO 4 layer on
476 the oxidation behavior of a directionally-solidified nickel-based superalloy at 850–900 °C, J Alloys
477 Compd 724 (2017) 565–574

478 [39] Y. Li, High-temperature oxidation, hot corrosion of five Ni-base superalloys and their protection,
479 Northeastern University, Shenyang, (2004) 35–38 (Ph. D. Paper)

480 [40] H. V. Pham, D. Maruoka, M. Nanko, Influences of Al_2O_3 grain size on high-temperature oxidation
481 of nano-Ni/Al2O3 composites, J. Asian Ceram. Soc. 4 (2016) 120-123

482 [41] H. Hindam, D. P. Whittle, Microstructure, Adhesion and Growth Kinetics of Protective Scales on
483 Metals and Alloys, Oxid. Met. 18 (1982) 245-284

484

485 **Figure captions**

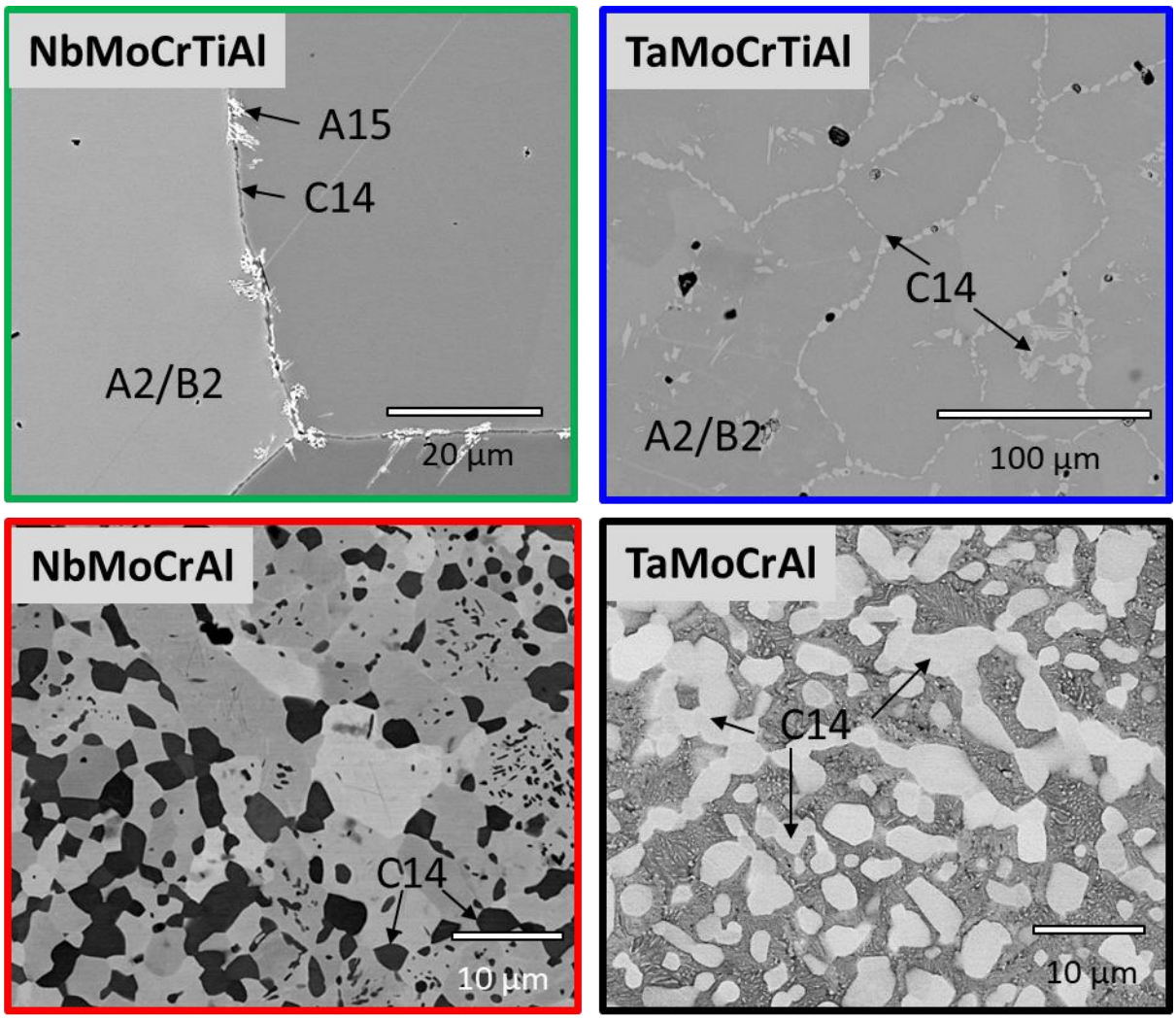

486

487 Fig. 1: BSE images of the investigated alloys TaMoCrTiAl, NbMoCrTiAl, NbMoCrAl and TaMoCrAl
488 after annealing conditions (see Tab. 1).

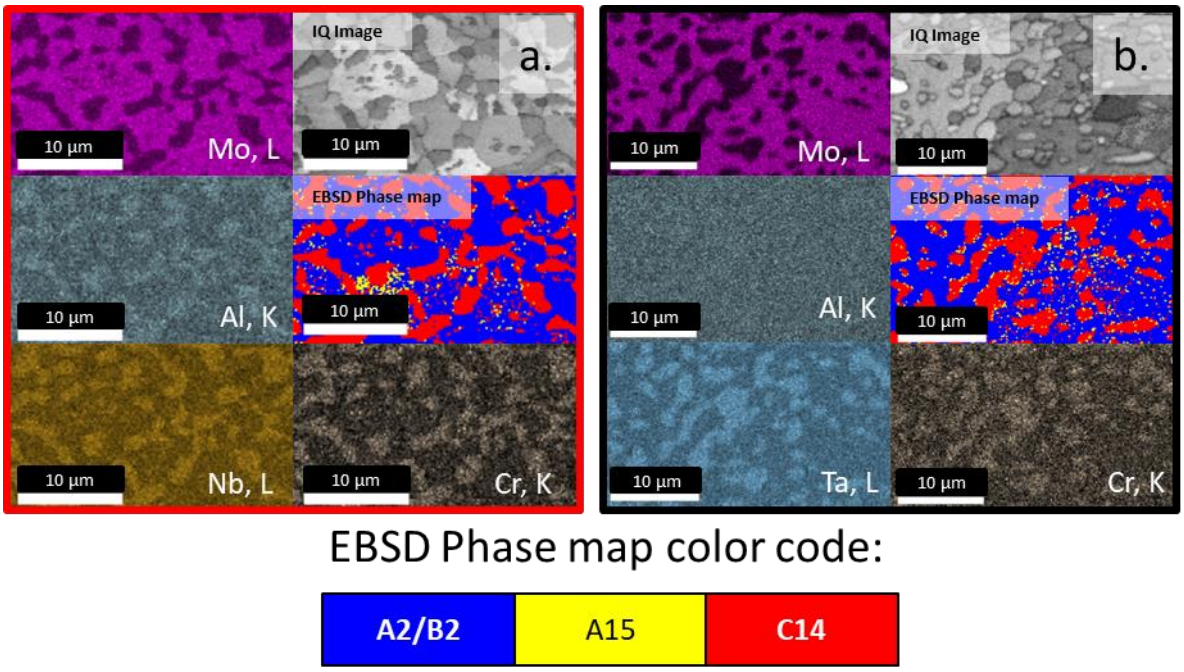

Fig. 2: Characterization of NbMoCrAl (a.) and TaMoCrAl (b.) by combined EDX and EBSD analysis

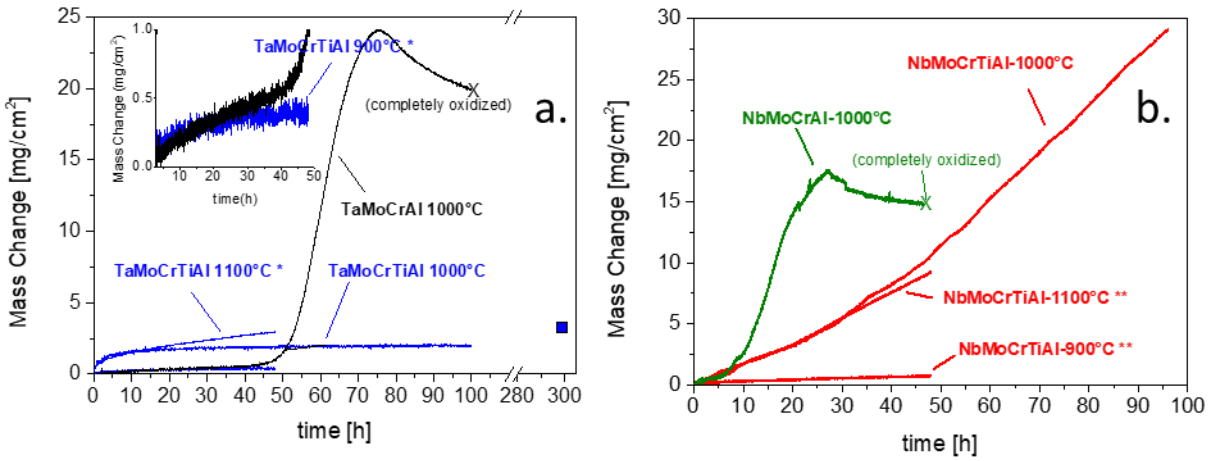

Fig. 3: Specific mass change as a function of time for TaMoCrTiAl and TaMoCrAl (a.) and NbMoCrTiAl and NbMoCrAl (b.) during isothermal exposure to air at 900 - 1100°C. Measurements denoted with * are taken from [11] and those with ** from [9].

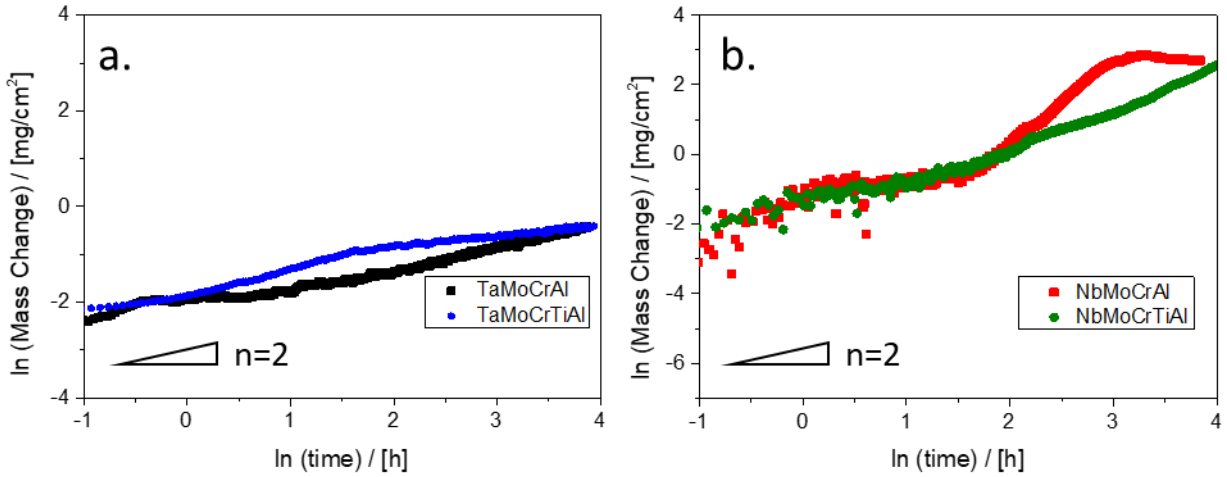

495

496 Fig. 4: Double logarithmic plots of mass change against time for TaMoCrTiAl, TaMoCrAl (a.) and for
497 NbMoCrTiAl and NbMoCrAl (b.) during isothermal oxidation at 1000°C in air up to 48h.

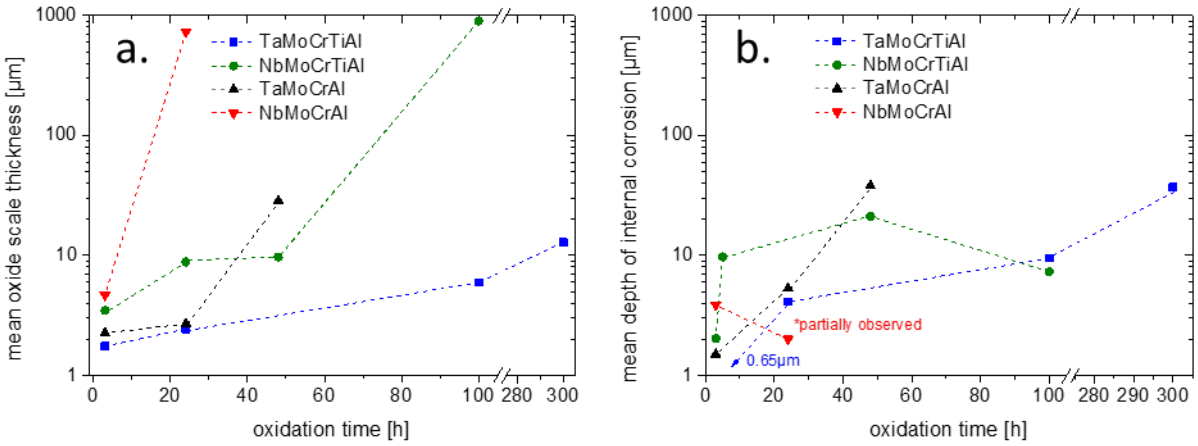

498

499 Fig. 5: Mean oxide scale thickness (a.) and mean depth of internal corrosion (b.) for TaMoCrTiAl,
500 NbMoCrTiAl, TaMoCrAl, and NbMoCrAl during isothermal exposure to air at 1000°C.

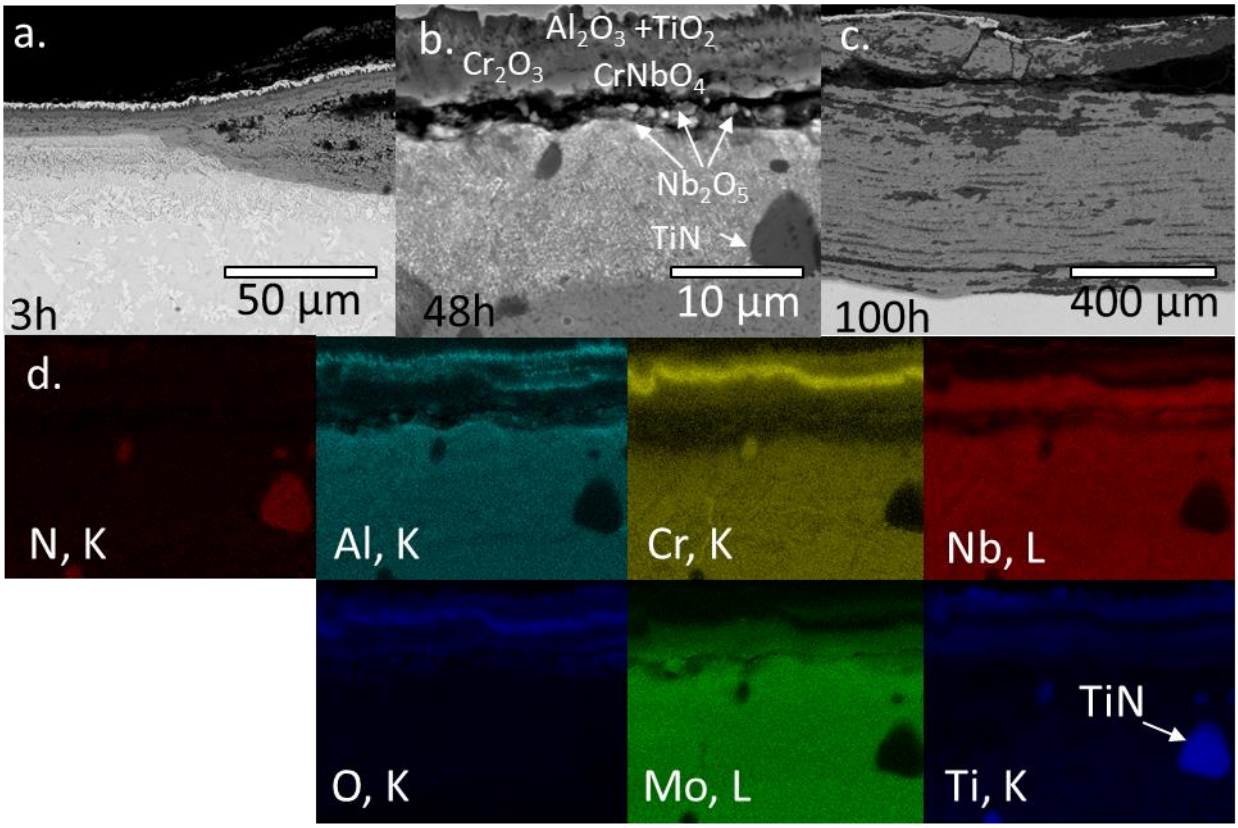

501

502 Fig. 6: BSE images of NbMoCrTiAl after 3h (a.), 48h (b.) and 100h (c.) of exposure to air at 1000°C
503 and (d.) the corresponding EDX-mappings of (b.).

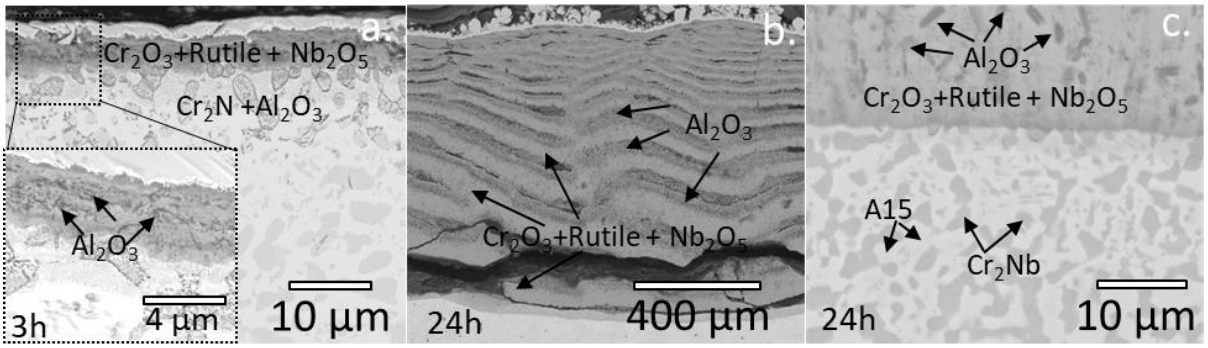

504

505 Fig. 7: BSE images of NbMoCrAl after 3h (a.) and 24h (b.) of exposure to air at 1000°C. A higher
506 magnification BSE image of the metal/oxide interface of (b.) is displayed in (c.).

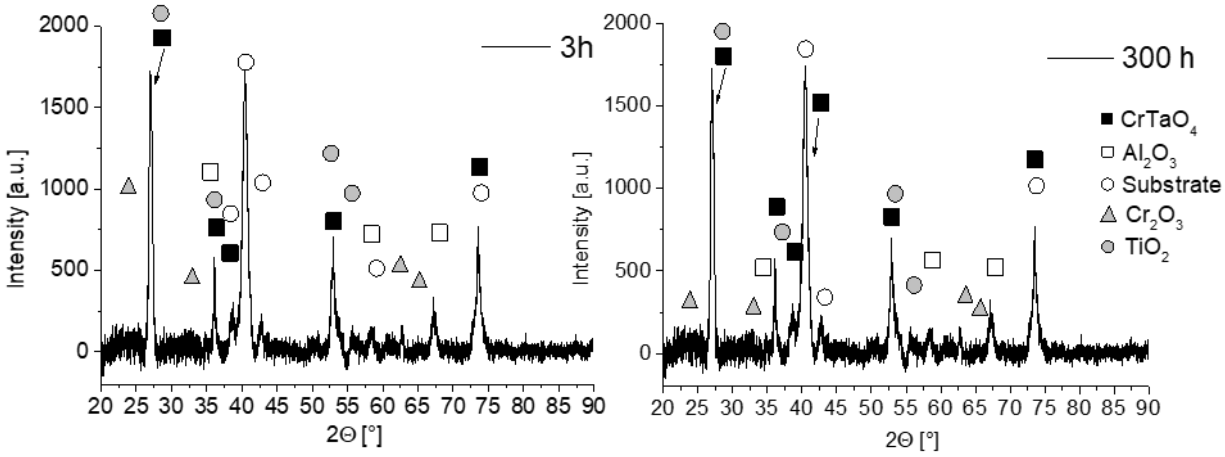

507

508 Fig. 8: XRD plots of TaMoCrTiAl after 3h and 300h oxidation at 1000°C in air.

509

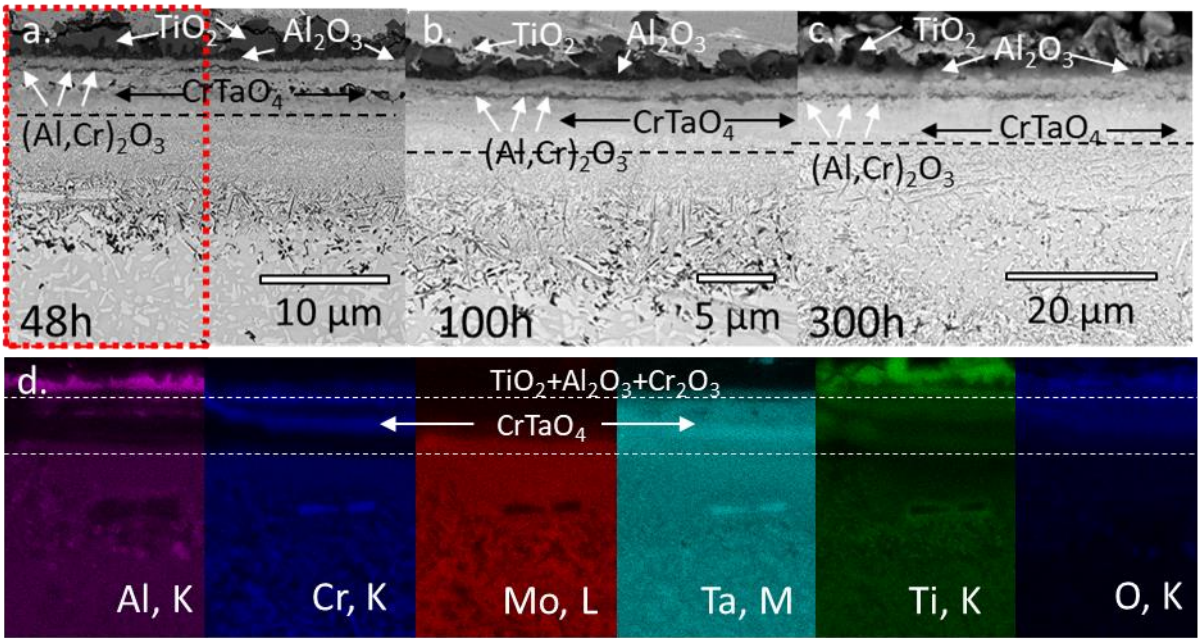

510

511 Fig. 9: BSE images of TaMoCrTiAl after 48h (a.), 100h (b.), 300h (c.) exposure to air at 1000°C and
512 EDX mapping (d.) of cross-section marked in (a.). The horizontal lines indicate the interface between
513 the oxide layer and the internal corrosion zone.

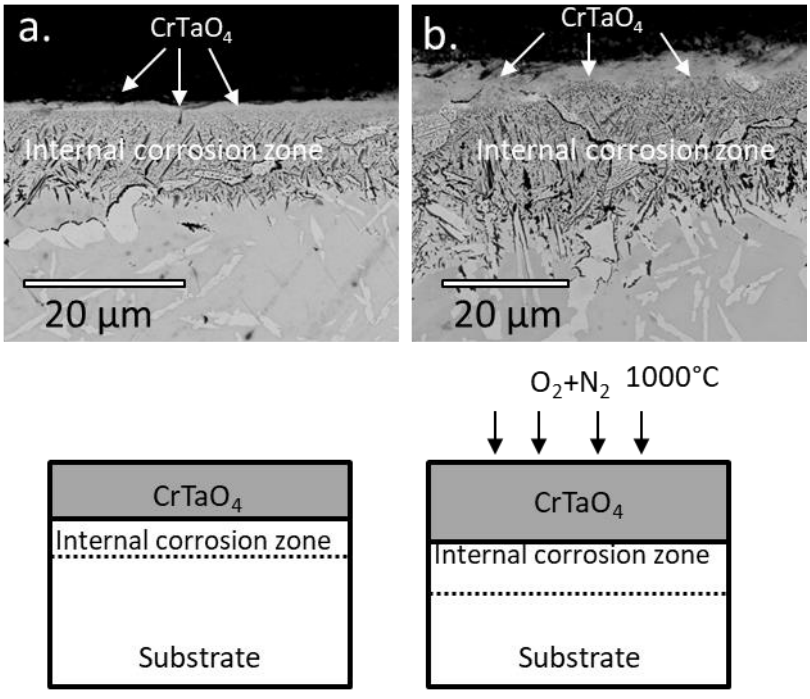

514

515 Fig. 10: Investigation of the protectiveness of the inner $CrTaO_4$ oxide layer during exposure to air at
516 1000°C. The darker upper oxide layer consisting of TiO_2, Al_2O_3 and Cr_2O_3 was removed, i.e. the $CrTaO_4$
517 is the outer oxide layer here (a.), after subsequent 24h oxidation at 1000°C in air no additional oxides
518 visible on top of $CrTaO_4$ (b.)

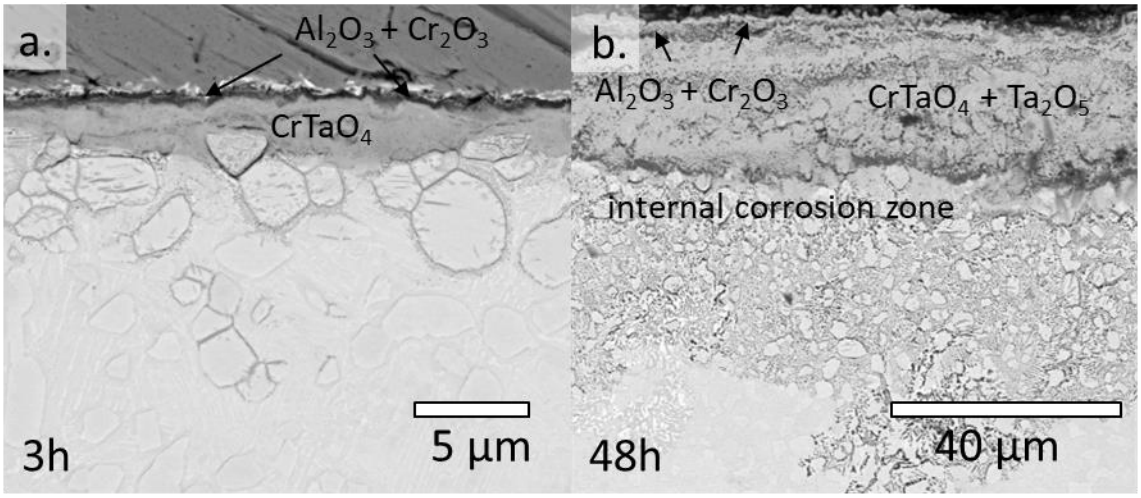

519

520 Fig. 11: BSE images of TaMoCrAl after 3h (a.) and 48h (b.) of exposure to air at 1000°C in air.

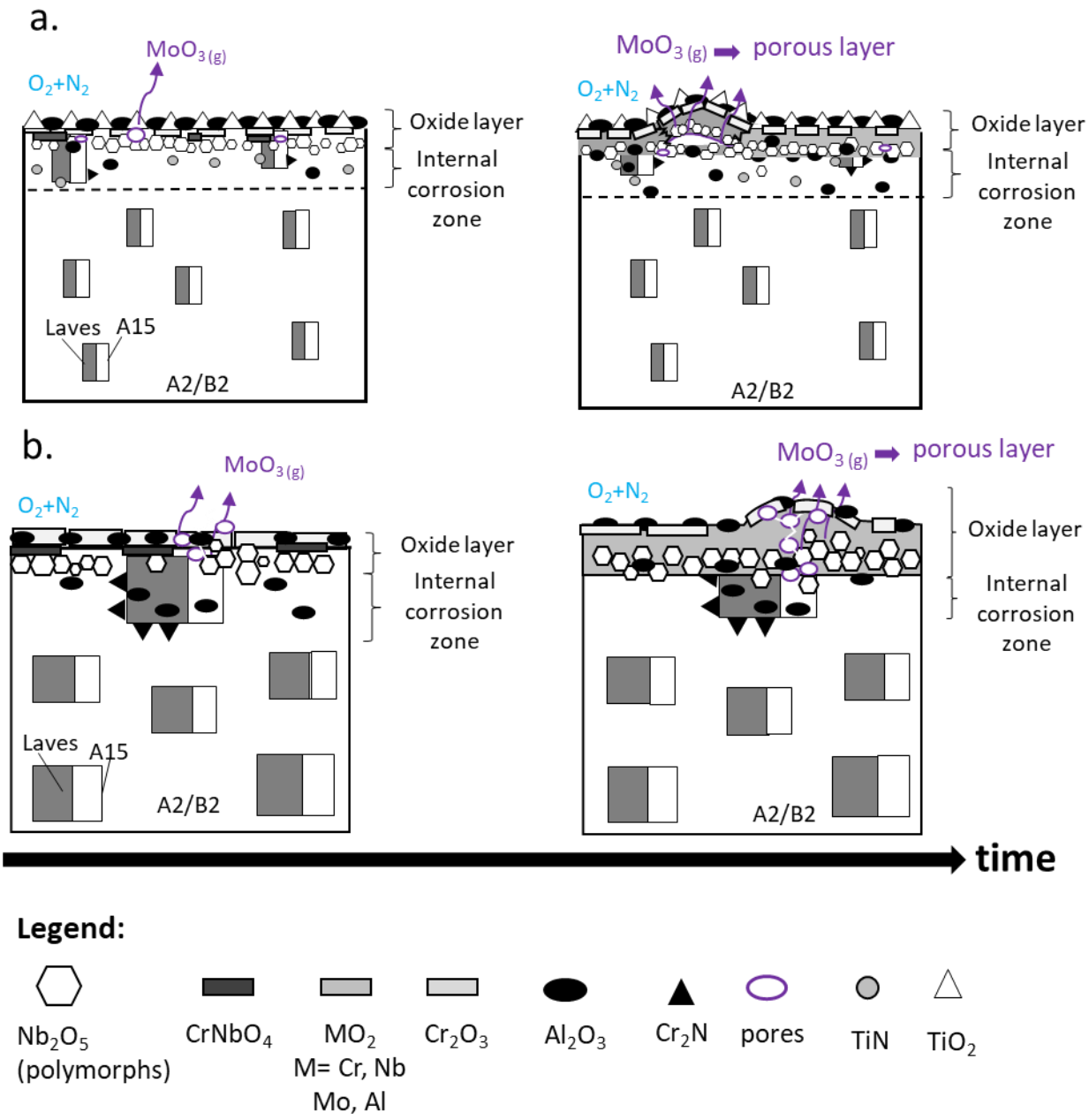

521

522 Fig. 12: Oxidation behavior of NbMoCrTiAl (a.) and NbMoCrAl (b.) during exposure at 1000°C in air

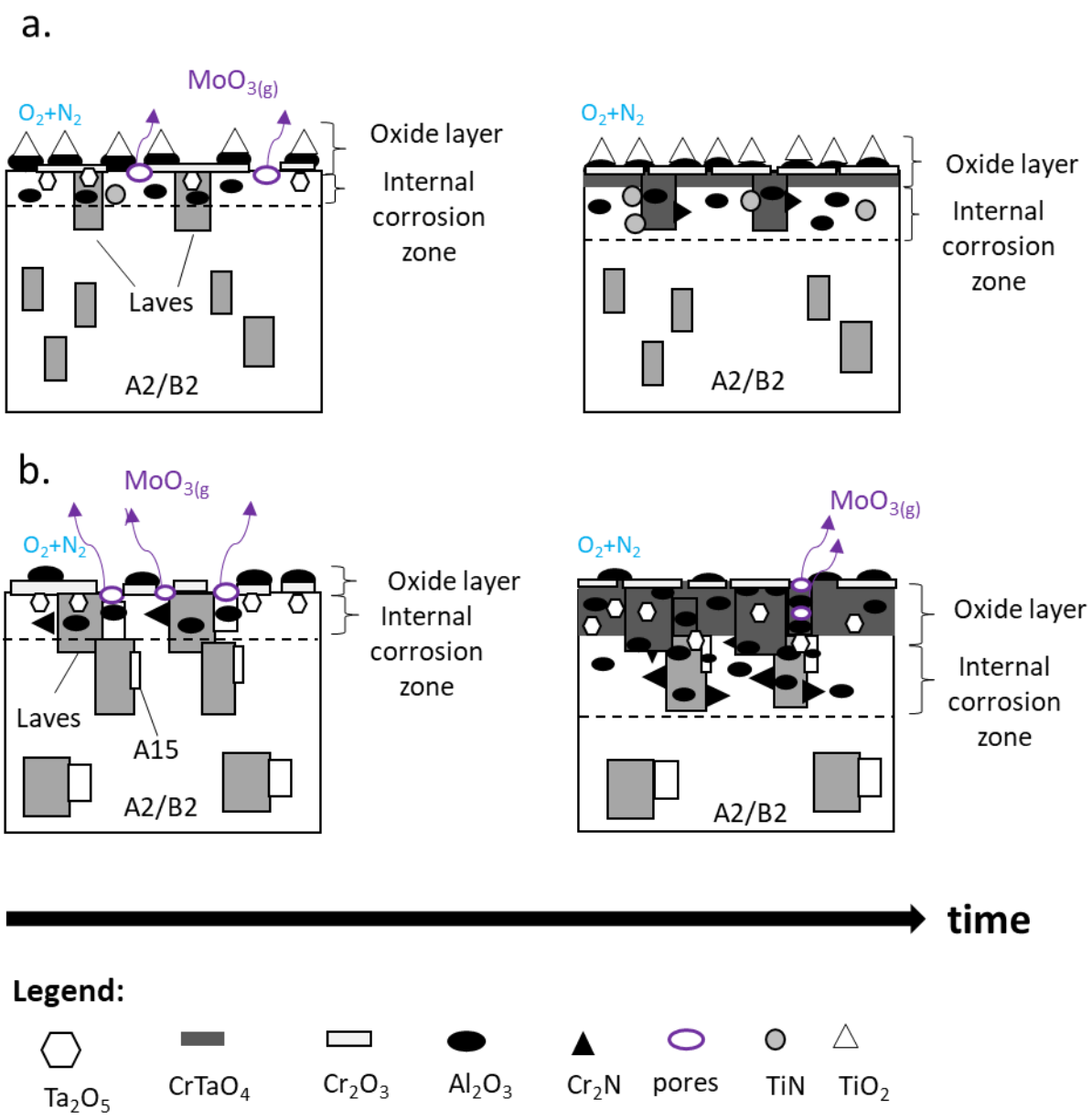

523

524 Fig. 13: Oxidation behavior of TaMoCrTiAl (a.) and TaMoCrAl (b.) during exposure at 1000°C in air

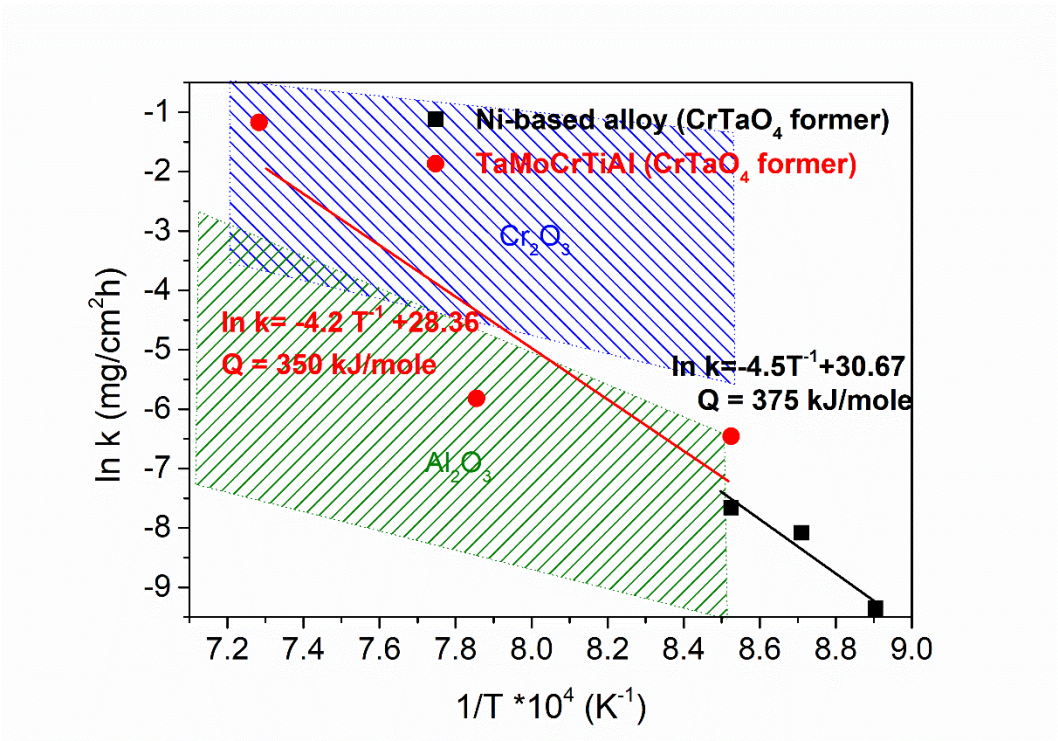

Fig. 14: Logarithm of the oxidation rate over reciprocal temperature during steady-state oxidation (after $CrTaO_4$ formation) of TaMoCrTiAl and $CrTaO_4$-forming Ni-based superalloy [39]. Scatter regions of oxidation rate for Al_2O_3 (olive shaded area) and Cr_2O_3 (blue shaded area) forming alloys after [41]

Table captions

Tab.1 Annealing conditions and identified phases of the investigated alloys. Volume fractions were accessed by means of BSE-contrast (denoted with *) or EBSD measurements (marked as †). The A2/B2 and A15 phases cannot be distinguished by means of BSE contrast or EBSD.

alloy	**annealing conditions**	**identified phases**	**area fractions /method**
NbMoCrTiAl	1300°C, 20 h	A2/B2 $Al(Mo,Nb)_3$ (A15) Laves phase, Cr_2Nb (C14)	99% * 0.5% * 0.5% *
NbMoCrAl	1300°C, 20 h	A2/B2+$Al(Mo,Nb)_3$ (A15) Laves phases, Cr_2Nb (C14)9	60% † 40% †
TaMoCrTiAl	1400°C, 20 h	A2/B2 Laves phases, Cr_2Nb (C14)	80% * 20% *
TaMoCrAl	1400°C, 20 h	A2/B2+$AlMo_3$ (A15) Laves phases, Cr_2Nb, (C14))	65% † 35% †

535 Tab. 2 Oxidation rate exponents (n) with regression coefficient (R^2) and oxidation constants (*k*)
536 calculated from the curves shown in Fig. 3

Alloy	**t_1 [h]**	**t_2 [h]**	**n**	**R^2**	**oxidation rate constant *k***
TaMoCrTiAl	0.4	4.5	1.82	0.99	$k_p=3.34\cdot10^{-2}$ [mg^2/cm^4 h^2]
	4.5	100.0	4.55	0.96	$k_q=2.97\cdot10^{-3}$ [mg^4/cm^8 h^4]
TaMoCrAl	0.4	3.0	4.35	0.96	$k_q=1.91\cdot10^{-4}$ [mg^4/cm^8 h^4]
	3.0	48.0	2.08	0.99	$k_p=7.96\cdot10^{-3}$ [mg^2/cm^4 h^2]
NbMoCrTiAl	0.4	8.2	1.49	0.97	$k_l=1.24\cdot10^{-1}$ [mg/cm^2 h]
	8.2	100.0	0.82	0.99	$k_l=3.45\cdot10^{-1}$ [mg/cm^2 h]
NbMoCrAl	0.4	7.6	2.08	0.95	$k_p=6.95\cdot10^{-2}$ [mg^2/cm^4 h^2]
	7.6	24.00	0.30	0.99	$k_l=1.12\cdot10^{-1}$ [mg/cm h]

537

538 Tab. 3 standard free energy of formation of relevant oxides at 1000°C

Oxide	**Cr_2O_3**	**Ta_2O_5**	**TiO_2 (rutile)**	**Al_2O_3**	**MoO_3**	**Nb_2O_5**	**$CrTaO_4$**	**$CrNbO_4$**
ΔG^0[kJ/mole O_2]	-538	-598	-713	-853	-293	-540	-568	-539

539

540

Supplementary Material

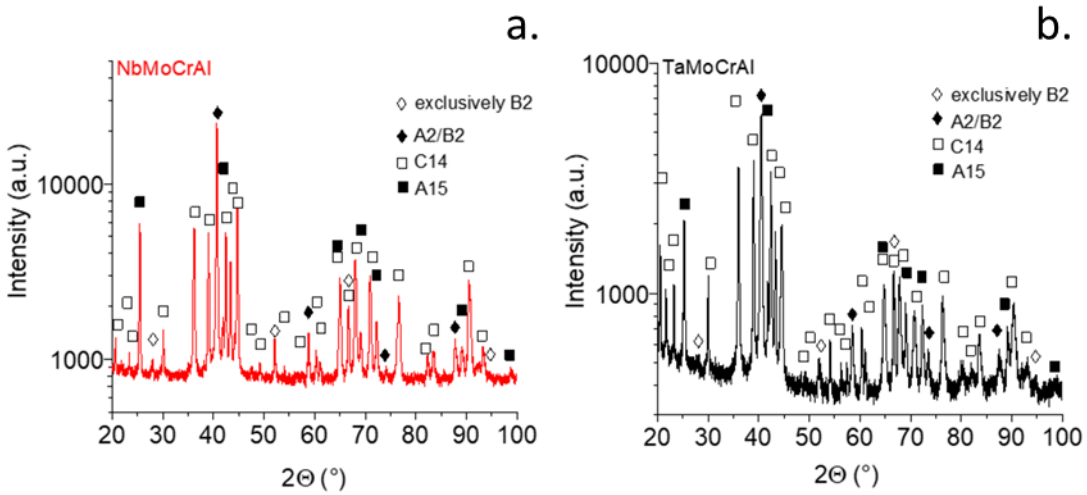

Fig. S1: Powder XRD patterns of NbMoCrAl (a.) and TaMoCrAl (b.). For better visibility of low-intensity peaks in the XRD, the intensity is plotted on a logarithmic scale.

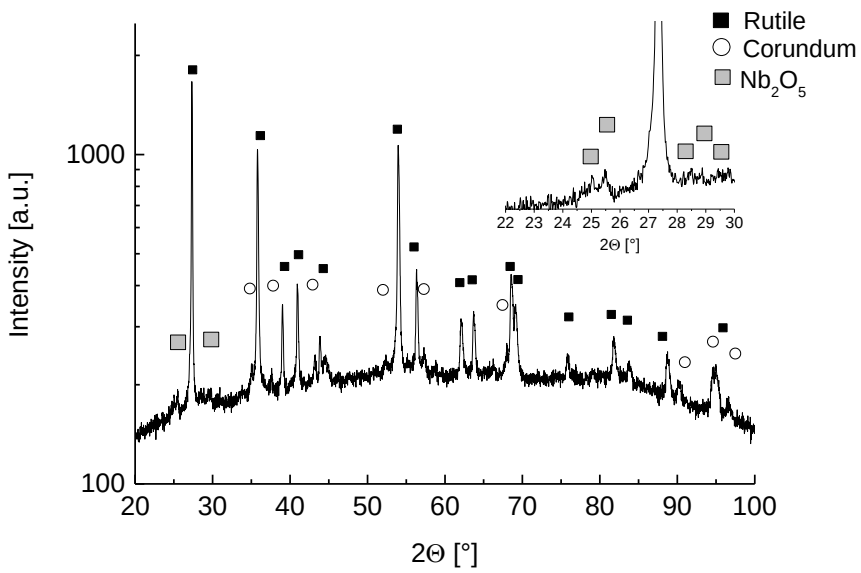

Fig. S2: Powder XRD analysis of the formed oxide scale of NbMoCrTiAl after 48h of exposure to air at 1000°C [9]. For better visibility of low-intensity peaks in the XRD, the intensity is plotted on a logarithmic scale.

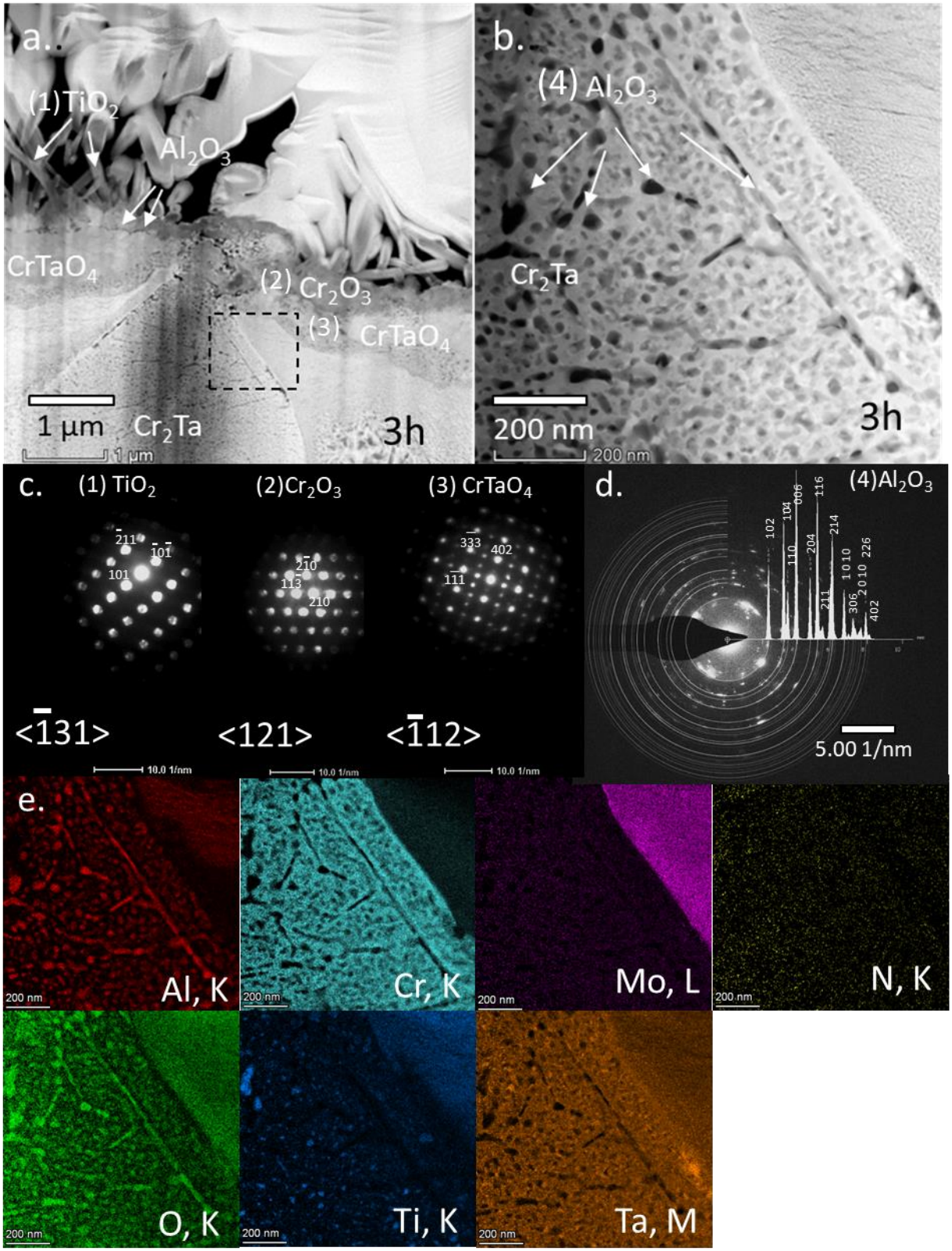

Fig. S3: STEM image (HAADF contrast) of TaMoCrTiAl after 3h exposure at 1000°C in air (a) as well as a magnification of the oxidized Laves phase (Cr_2Ta) in (b.). TEM diffraction pattern of the marked oxides in (a.). TEM ring diffraction pattern of Al_2O_3 (d.). EDX mapping of Fig. (b.) (e.).

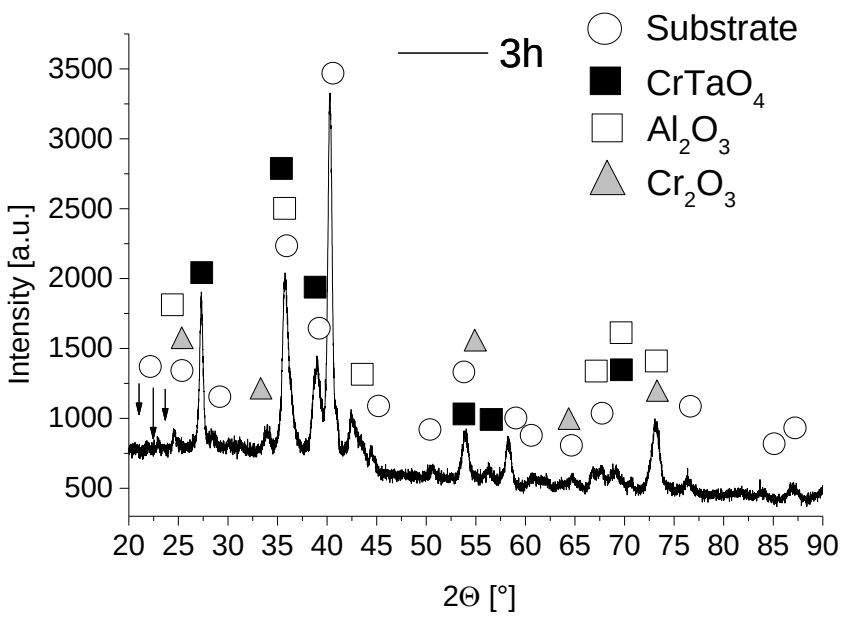

558

559 Fig. S4: XRD measurement of TaMoCrAl after 3h exposure to air at 1000°C

560

561